Intermittent microplasticity in the presence of a complex microstructure

Q. Rizzardi,[1] P. M. Derlet,[2] and R. Maaß [1,3,*]

[1]*Department of Materials Science and Engineering, University of Illinois at Urbana-Champaign, Urbana, Illinois 61801, USA*
[2]*Condensed Matter Theory Group, Paul Scherrer Institute, 5232 Villigen PSI, Switzerland*
[3]*Federal Institute of Materials Research and Testing (BAM), Unter den Eichen 87, 12205 Berlin, Germany*

We demonstrate the gradual shift from scale-free intermittent microplasticity to a scale-dependent behavior via the introduction of a variety of microstructural features within the Al-Cu binary alloy system. As long as the obstacles to dislocation motion remain shearable, the statistics of intermittent microplasticity has fat-tailed contributions. The introduction of incoherent precipitates leads to a complete transition from scale-free power-law scaling to an exponential and scale-dependent distribution. These results demonstrate how non-Gaussian interactions survive across different microstructures and further suggest that characteristic microstructural length scales and obstacle pinning-strengths are of secondary importance for the intermittency statistics, as long as dislocations can shear their local environment.

I. INTRODUCTION

That plastic flow of crystals can proceed both smoothly and intermittently is a long-known realization in materials science and materials physics. Almost 100 years ago, when the foundations for today's crystal plasticity were laid by Orowan, Becker, Valouch, Schmid, and many others, it was already recognized that pure single crystals can, under certain conditions, exhibit an overall flow response that was composed of smooth continuous stress-strain segments, intermixed with abrupt stochastic strain jumps [1–3]. This bimodal mechanical response originates from strain localization where, in addition to homogeneous flow, large plastic events intermittently occur and lead to discrete plastic strain events. Despite the coexistence of smooth and intermittent plasticity in one and the same material, approaches that homogenize plastic flow were successfully developed and are still used today. A prominent and simple example is the Orowan equation, $\dot{\gamma} = b\rho\bar{v}$, where $\bar{v}$ and ρ are related to average quantities that implicitly assume some Gaussian statistics over a large representative volume element, or simply the tested material. Exceptions to the norm of homogeneous plastic flow (or viscous flow [4]) of pure metals have sporadically been reported in the literature, where either remarkable instrumentation with very high strain resolution was used [5], or sensitive acoustic emission methods [6] revealed a fundamentally intermittent dislocation process that must underlie the stochastic strain increments or pulse-energy excursions.

Today, the spatiotemporal nature of intermittent plastic flow is an established concept and in fact is seen in a variety of bulk-scale experiments [7–9], and is essentially the norm in small-scale mechanical testing [10–14]. Progress in understanding the intermittent rearrangement of the mediating dislocation network was mainly made via a statistical assessment of either acoustic emission pulses [15] or stress-

strain increments [16], revealing non-Gaussian behavior in the form of perfect power laws, $P \sim S^{-\tau}$ [17] or exponentially truncated power laws, $P \sim S^{-\tau}e^{-L/S}$ [18,19], where S is the event size, P the probability of the event occurring, and L a material-specific length scale. Such statistical signatures of the occurring events S represent a paradigm shift away from classical homogenization schemes [20] and indicate divergent length scales over which the rearranging dislocation network couples and collectively responds to relax internal stresses. Both mean-field modeling of avalanches near the depinning transition in the presence of a static pinning field [21] and dislocation dynamics simulations interpreting the stochastic evolution of a line-defect population as a jamming-unjamming [22,23] transition have given analytical insights into the scale-free statistics of intermittent plasticity.

Intriguingly, statistical divergence in the form of power-law scaling can persist for microstructures with internal length scales [3] and across grain boundaries [7], but it has also been shown that the introduction of deformation substructures can decrease S, which truncates $P(S)$ without affecting τ [19], or that both the truncation and the scaling exponents are affected by obstacles [24,25] or grain boundaries [26]. Very recent work on $P(S)$ further demonstrated how power-law truncation of micron-sized crystals is not linked to a finite size effect, but rather to the degree of how collective dislocation activity localizes spatially [27]. In other words, L/S is linked to an internal length scale instead of the finite crystal dimension. Similarly, the scaling exponent τ can be sensitive to the presence of strong obstacles, as revealed with discrete dislocation dynamics, where the strength and distribution of static pinning fields [22,28] or the ratio of average precipitate size to sample diameter can be varied [25,29]. Being convoluted with a variety of other effects, such as external size variation, strain-rate effects, and different microstructural obstacles, direct comparisons are difficult. These scattered and partially inconsistent observations therefore prompt the question of what relationship there may be between an internal microstructural length

*robert.maass@bam.de

TABLE I. Heat treatments applied to each sample to obtain the desired microstructure. These microstructures were all confirmed via TEM analysis.

Microstructure	Heat treatment
Solid solution (AlCuSS)	Room temperature water quench (WQ)→stored at 273–278 K
GP zones (AlCuGP)	WQ→Naturally aged (NA) at room temperature (293 K)
θ'' (AlCuθ'')	WQ→Artificially aged for 30 h at 453 K
θ'/θ (AlCuθ'/θ)	WQ→Artificially aged for 200 h at 453 K

scale on one side, and the scaling exponent or the truncation length scale on the other side.

To shed more light onto this question, we probe here the intermittent plasticity of pure Al and a binary Al-Cu alloy, which serve as model materials, where the alloy offers a tunable microstructure depending on its annealing history, spanning from a solid solution to a population of unshearable θ'/θ precipitates. From a materials physics perspective, this choice of crystals encompasses a structure admitting jamming-unjamming transitions in the case of pure Al and a variety of microstructures in which pinning-depinning dynamics is expected due to the different populations of shearable and unshearable obstacles in the binary alloy. Across the different microstructures but identical deformation rates and external sample sizes, a gradual truncation of the avalanche statistics from a truncated power law to a finite valued distribution is revealed when transitioning from pure Al to a θ'/θ-precipitate-containing structure. The introduction of a solid solution causes a pronounced increase of small avalanches, but the avalanche statistics continues to have a power-law-like tail, albeit of lower probability than for the pure Al crystal. Quantifiable length scales of the sampled microstructures do not yield any immediate rationale for the changes in intermittency statistics, and the loss of the extreme-value tail emerges due to the formation of unshearable θ'/θ precipitates.

II. EXPERIMENTAL METHODS

Microcrystals were produced from a pure bulk Al polycrystal (99.995%, provided by Teck Products) and from a bulk polycrystalline Al 4.85 wt % Cu alloy produced by Goodfellow. Hereafter we will refer to AlCu samples for simplicity instead of Al 4.85 wt % Cu. All samples were mechanically polished to a mirror finish prior to microcrystal extraction. To ensure full dissolution of Cu in the Al matrix, the binary alloy was homogenized for 90 h at 813 K. Subsequent to homogenization, different bulk pieces of the AlCu underwent specific heat treatments to generate precipitation microstructures, as summarized in Table I.

All microstructures (including pure Al) were characterized via electron backscattered diffraction (EBSD) in a JEOL 7000M scanning-electron microscope (SEM). Grains were found to be equiaxed and randomly oriented, with average diameters ranging between 50 and 500 μm. For each microstructure, a grain oriented as close as possible to the [001] direction (with misorientations $\leqslant 5°$ and accounted for when calculating Schmid factors) was selected for transmission-electron microscope (TEM) analysis and microcrystal preparation. TEM lamellae were extracted either in a

FEI Helios 600i Dual Beam SEM/FIB (focused ion beam) or a Thermo Scios2 Dual-Beam SEM/FIB. The lamellae were analyzed in a JEOL 2010 LAB6 TEM to study dislocation and precipitate structures. Additional lamellae were extracted *ad hoc* and subsequently analyzed to ensure statistical significance when determining precipitate size and spacing, as well as dislocation density.

Microcrystals of cylindrical shape, with a height of 6 μm and a diameter of 2 μm, were carved into the identified grains via FIB milling. The final tapering angle along the length of each microcrystal was evaluated to less than 1°. A craterlike zone, 35 μm in diameter, was left around each microcrystal to allow mechanical loading of the microcrystal without contacting the bulk of the crystal. The microcrystals were mechanically stressed under uniaxial compression with the use of an 11 μm diameter flat punch indentation tip affixed to a TI-950 Bruker-Hysitron nanoindenter. The compression experiments were displacement controlled at a constant rate of 0.6 nm s^{-1} over a total displacement per experiment of 150 nm, which corresponds to a strain rate of 10^{-4} s^{-1}. The total compression displacement for each microcrystal was set as 1500 nm, i.e., ten individual loading experiments per microcrystal. The data acquisition rate was limited by the indenter's internal memory but was at least 800 Hz for all experiments.

The data output of the experiments is simple arrays containing time, depth, load, and corresponding voltages. All data files were processed via a series of MATLAB routines. First, the slope of depth over time is output as an approximation for the quasistatic deformation response, where intermittent plastic events are detected by an abrupt increase of the moving slope. Second, selected event segments are manually reviewed and either kept as intermittent plasticity events or discarded as noise, the definition of which will be addressed later. Third, each event is bound in time and its depth/force trace is denoised by Wiener filtering. Once filtered, the peak velocity of the event is established, and new time bounds are set up where the momentary deformation velocity reaches 10% of the peak velocity on each side of the peak. The resulting events have a filtered depth, time span, and velocity profile, and are statistically analyzed using the PYTHON maximum likelihood estimation (MLE) method that is part of the POWERLAW package developed by Alstott *et al.* [30].

Given the relatively small magnitude of some of the resulting intermittent plasticity events (less than 0.5 nm; see Fig. 5), particular care went into establishing a noise threshold. To this end, the AlCuθ'/θ sample was placed in the TI-950 under a load of 200 μN (well within the elastic domain of the sample) for a duration of 5 min, to obtain recordings of the background noise during experimentation. The background noise was
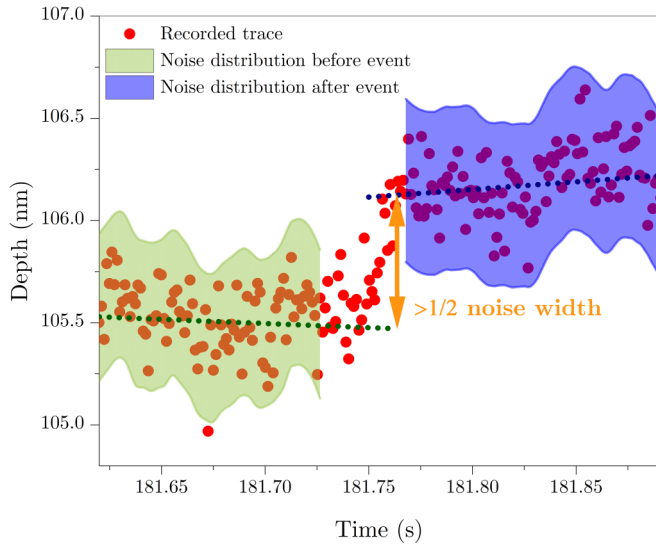
FIG. 1. An example of a real data trace of an event for AlCuθ'/θ. An envelope of two standard deviations indicates the data distribution on both sides of the event. Since the change in the data distribution overall shifts to higher depth by more than half of the enveloped standard deviations, the event is detected as real. Here the example event has a final magnitude of ca. 0.6 nm.

found to follow a normal distribution with $\mu = 2 \times 10^{-5}$ nm (which can be approximated as zero) and a standard deviation $\sigma = 0.23$ nm. However, this distribution returns the absolute displacement between two consecutive points, which is not necessarily applicable to intermittent plastic behavior, which is expected to consist of a sustained increase in depth over several data points, as highlighted in Fig. 1. Here, the data points before and after the event were separated, their respective noise distributions were calculated, and a data "envelope" corresponding to a distance of $\pm 2\sigma$ from the data mean was determined. If the envelopes before and after the event show a shift of at least half their width, it is considered that a plastic event has occurred beyond a reasonable doubt. Following this approach, the detection threshold for events was determined to be 0.17 nm. Consequently, only events whose size S exceeds the threshold have been considered in the following.

III. RESULTS AND DISCUSSION

Figures 2(a)–2(e) show the TEM micrographs of the actual microstructures, while Figs. 2(f)–2(j) show a schematic of the expected idealized microstructures of each structural state. The microstructures are described as follows: Panels (a,f) show pure and well-annealed aluminum with a dislocation density of ca. 5×10^{12} m^{-2}. No precipitates or dislocation braids could be identified. Panels (b,g) show AlCuSS, a substitutional solid solution of copper in an aluminum matrix. The nominal composition of the alloy is 4.85 wt % Cu, which is below the maximum solubility of Cu into Al near the eutectic temperature (821.4 K), but results in a supersaturated solid solution once quenched to room temperature. In order to avoid room temperature aging, all samples of this microstructure were stored after quenching at a temperature of 273–278 K. Panels (c,h) show AlCuGP-containing Guinier-Preston (GP) zones in an AlCu matrix. GP zones are a well-known transitional structure encountered during precipitate growth in AlCu samples at room temperature. They consist of local concentrations of copper atoms that segregate into energetically favorable configurations following random diffusion. These configurations are AlCuθ'', small disks aligned on {001} planes with a diameter of approx. 1−10 nm, and a thickness of up to a few atomic layers. Seen edge-on as is the case in Fig. 1(c), they appear as thin line contrasts only visible once atomic resolution is reached. Panels (d,i) show a structure of θ'' precipitates that correspond to the next precipitation stage in AlCu alloys. θ'' precipitates (also known as GP II) are fully coherent with the matrix; the literature shows that they are formed by Cu substitution on the fcc lattice sites at a distance of three atomic planes and create a tetragonal structure [31]. They are the continuation of the Cu agglomeration process initiated with GP zones and are disks with a diameter of 10−100 nm, a thickness of 5−10 nm, and again visible viewed edge-on, although circular regions of darker contrast could also be identified in the structure as the θ'' phase seen from their face side. Panels (e,j) show that AlCuθ'/θ is a structure containing the final stages of precipitation in AlCu alloys, namely, θ' and θ precipitates. Unlike θ'' precipitates which grow directly out of GP zones, θ' precipitation can occur not only on GP/θ'' structures, but also on defects like dislocations and low-angle grain boundaries. θ' precipitates are metastable and associated with a loss
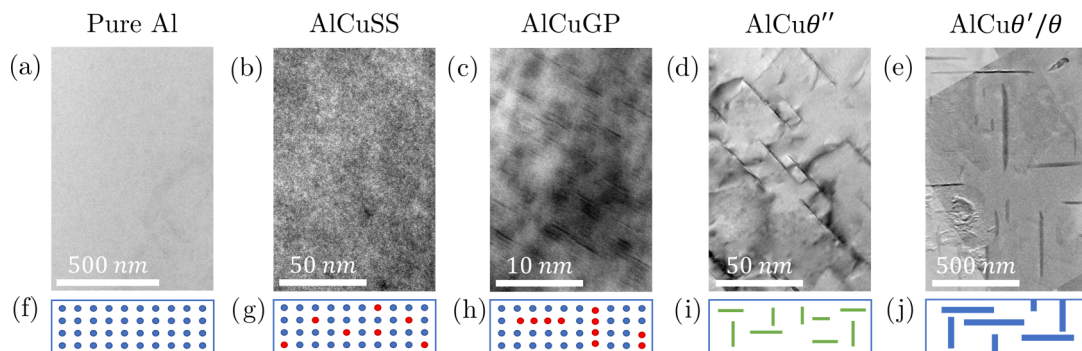

FIG. 2. The top row (a–e) displays representative TEM micrographs of all probed microstructures and the bottom row (f–j) schematically visualizes the structures.
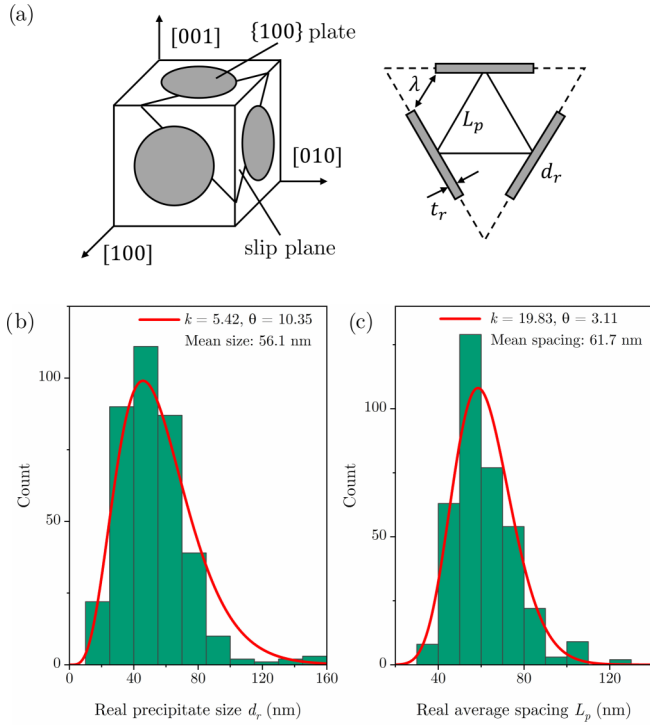
FIG. 3. (a) Schematic describing the relationship between the measured quantities on {001} planes and the quantities as seen on the {111} slip plane family relevant for dislocation-precipitate interaction. (b) Histogram of precipitate size d_r for AlCuθ''. (c) Histogram of precipitate spacing L_p for AlCuθ'' as defined in (a). For both distributions, the best fit is given by the gamma distribution and allows determining a mean value.

TABLE II. Real precipitate dimensions based on measured values during TEM analysis, as well as pinning strength τ_{pin} and corresponding characteristic length l as defined in Ref. [24].

Structure	d_r (nm)	t_r (nm)	L_p (nm)	λ (nm)	τ_{pin} (MPa)	l (nm)
Pure Al	–	–	–	–	–	–
AlCuSS	–	–	2.1	2.1	106.7	67.0
AlCuGP	3.5	0.3	4.3	2.6	68.6	104.2
AlCuθ''	56.1	6.1	61.7	30.4	92.1	77.6
AlCuθ'/θ	437	19.1	365	173	58.0	123.2

ings, which are relevant when discussing dislocation motion on the {111} plane. The translation of measured dimensions into real length scales of the 3D microstructure has been established before by Nie and colleagues [36,37], and proven accurate [38–40]. Following Ref. [25], the real average diameter of the precipitates d_r is given by

$$d_r = \frac{2}{\pi}[d_m - t_f + \sqrt{(d_m - t_f)^2 + \pi d_m t_f}], \qquad (1)$$

where d_m is the average measured diameter, and t_f the TEM foil thickness. Determining the precipitate thickness is straightforward since the TEM micrographs are obtained using a [001] zone axis. The real thickness t_r can be shown to be $t_r = t_m \sin 54.74°$, with t_m the mean measured thickness and the $54.74°$ angle corresponding to the angle between the {001} and the {111} planes. Finally, we determine the average distance between precipitates that dislocations would encounter on the {111} planes, being L_p and λ. As per the calculations detailed in Refs. [25,36], both distances can be related to precipitate size according to

$$\lambda = L_p - \frac{d_m}{2} - \frac{\sqrt{3}}{2}t_m = \frac{1.030}{\sqrt{N_v d_r}} - \frac{\pi d_r}{8} - \frac{\sqrt{3}}{2\sin 54.74°}t_r, \qquad (2)$$

with N_v is the precipitate density. The results for d_r, t_r, L_p, and λ were compiled in histograms if applicable for the studied microstructures. For all histograms, the best fit to the data was found to be a gamma distribution [example fits are displayed in Figs. 3(b) and 3(c)], whose probability distribution function is of the form $f_x = \frac{x^{k-1} e^{-\frac{x}{\Theta}}}{\Theta^k \Gamma(k)}$ with k and Θ being fitting parameters. The mean values, $x_m = k\Theta$, for the quantified length scales are listed in Table II. In the case of AlCuSS, λ and L_p are replaced by the average spacing between nearest-neighbor copper atoms based on the assumption of a homogeneous distribution of the atoms within the matrix. The values of Table II are consistent with similar studies [32,38,41], with roughly one order of magnitude difference in precipitate size and spacing between AlCuGP, AlCuθ'', and AlCuθ'/θ.

An engineering stress-strain curve of each microstructure type is shown Fig. 4(a). The strong variation in initial loading slope is a convolution of alignment imperfections and drift rates and should not be used for modulus estimations [42]. However, the flow regime is a robust plastic response of the material. Each flow curve exhibits stress-strain instabilities of different degrees that are separated by smooth deformation-curve segments. The abrupt strain increments are caused by collective dislocation rearrangements or

of coherency. The precipitates are still disk shaped on the {001} planes, with diameters ranging between $100-500$ μm and having a thickness of $15-40$ nm. θ precipitates are seen once the aging results in primarily incoherent precipitates that depart from the previous disk shape. Their size may also exceed that of the θ' phase. While previous structures contribute to strengthening via shear mechanisms, the presence of θ'/θ induces a change from precipitate shearing to Orowan looping. These precipitates have been extensively described in the literature [32–35], but their description of a relatively continuous growth process as separate categories brings some ambiguity when considering transition structures that do not fall squarely into one category. It should be noted that the precipitates are not expected to entirely exhaust the supply of Cu of the system, leaving dissolved copper in the Al matrix in all the AlCu microstructures.

To quantify the potential effect of internal length scale on the statistical signature of plastic fluctuations, it is paramount to carefully determine both the dimensions and spacing of the precipitates. To this end, a series of TEM lamellae were extracted from the GP, θ'', and θ'/θ microstructure and evaluated.

Before performing any quantitative analysis of the length scales derived with TEM, it is imperative to realize that they originate from a two-dimensional (2D) projection. Figure 3(a) shows the real shape and distribution of the precipitates, as well as their center-to-center (L_p) and edge-to-edge (λ) spac-
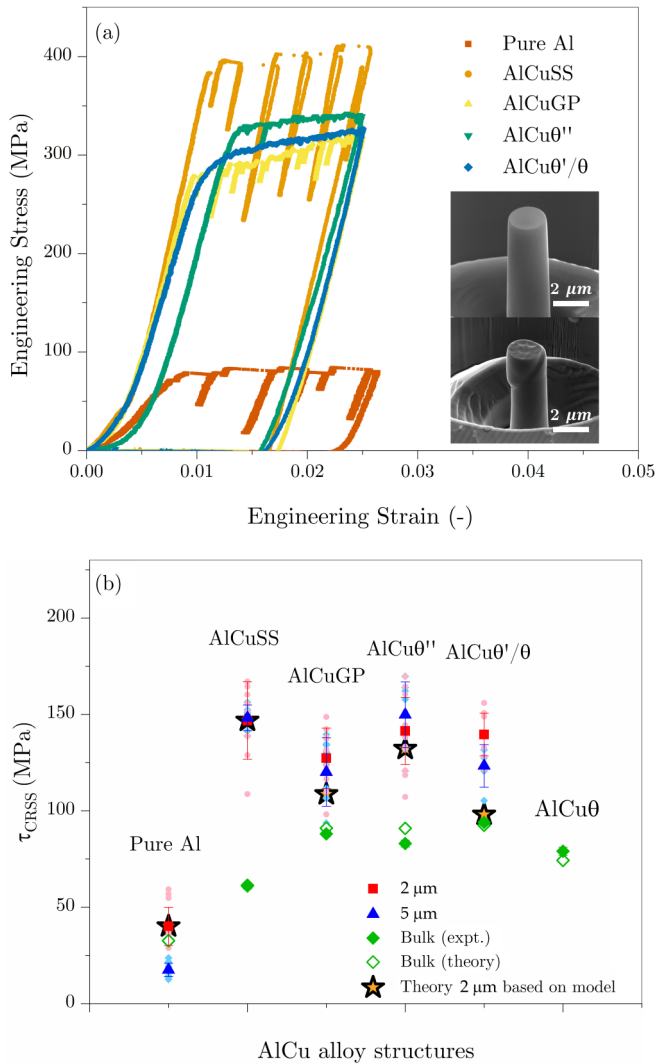
FIG. 4. (a) Measured engineering stress-strain curves for each sample microstructure. The addition of Cu results in a noticeable increase in flow stress. Inset: SEM micrographs of a pure Al microcrystal before and after microcompression. The sharp slip trace is the expected behavior for an fcc structure. (b) Critical resolved shear stress, τ_{CRSS}, for each different microstructure, measured on microcrystals of diameter 2 and 5 μm. Unlike the tendency observed in the bulk in the literature, the highest τ_{CRSS} are measured for the AlCuSS structure. The bulk theoretical and experimental values of Ref. [38] are included for comparison purposes.

dislocation avalanches, which are known to be dominated by the activation of single-armed dislocation sources that lead to the formation of visible slip offsets [inset in Fig. 4(a)] [43]. Qualitatively, the stress-strain curves reveal a gradual reduction of intermittency as the precipitate size increases. Such a change in intermittency has experimentally been discussed in the context of microcrystal size [44] and precipitate-microcrystal size ratio [25], whereas the effect of a varying disorder strength of a static pinning field—here represented by the microstructural deviations away from pure Al—has so far been limited to two-dimensional dislocation dynamics simulations [45]. Before quantifying the change in intermittency due to different types of internal pinning sites and characteristic

length scales, we turn our attention to the strength variation across microstructures, which is summarized and compared to corresponding bulk experiments [38] in Fig. 4(b).

Given the typically large scatter in strength at the micron scale, the measured critical resolved shear stress, τ_{CRSS}, during the flow regime of more than ten microcrystals has been averaged for each alloy. Figure 4(b) displays data points for individual microcrystals and their average values for both 2 and 5 μm diameter samples. The reason for also testing larger microcrystals will be addressed later. As expected, the pure Al crystals exhibit the well-known finite sample-size effect due to dislocation sampling statistics, source hardening, and exhaustion hardening [46,47]. Introducing Cu to Al, a substantial jump in τ_{CRSS} is seen for all AlCu microstructures, but within the spread of individual measurements, no justifiable difference in strength between them can be derived. Irrespective of AlCu microstructure, the average shear flow stress attains a level of 130–150 MPa with a spread of around 50 MPa indicating no gradual increase in strength as known for the bulk microstructures that continuously become stronger towards the AlCuθ'/θ and weaken with the dominance of θ due to increasing Orowan looping. This classically known behavior of peak aging [35,48,49] is captured by the bulk data contained in Fig. 4(b) for an AlCu 4.2% binary.

To better compare the strength difference between the microcrystals and the expected bulk values, we use the same theoretical strength model underlying the bulk data in Fig. 4(b) [38]. This model relies on summing the different strengthening contributions of each microstructural feature to a base strength of pure Al. For the solid solution, the strengthening contribution is given by $\tau_{ss} = HX_{Cu}^n$, with X_{Cu} being the weight fraction of Cu dissolved as a solid solution in the Al (here 4.85 wt %), and H and n constants found to be 22 MPa and 1, respectively, for Al-Cu binary systems [50]. The contribution of precipitates is a bit more complex and depends largely on their geometry, orientation, and shearability. GP zones, in particular, have proven hard to be modeled and instead rely on a simplification, where GP zones are assumed to be spheres of diameter d, according to

$$\tau_{GP} = \frac{1}{b}\sqrt{\frac{3f}{2\pi}}(0.72Gb^2)\left(\frac{2}{d_c}\right)^{1.5}\left(\frac{d}{2}\right)^{0.5}, \quad (3)$$

where $d_c = 20$ nm and $f = \frac{d_r^2 N_v \pi}{4}t_r$ [37]. The above model is only valid if the GP zones' diameter $d < d_c$, which as per Fig. 2 is the case. θ'' precipitates are treated as circular plates on {001} planes and we expect them to be weak enough to be sheared on the {111} planes, in which case the corresponding strengthening contribution has been described by [51]

$$\tau_{\theta''} = \frac{0.908d_r}{(t_r)^2}\left(\frac{2\pi bf}{Gb^2\ln\sqrt{\frac{d_r^2}{2b^2f}}}\right)^{0.5}\gamma^{1.5}. \quad (4)$$

Here, γ is the interfacial energy between the matrix and precipitates, evaluated to be 154 mJ m^{-2} [38]. Finally, θ' and θ precipitates are too large and incoherent to allow shearing; instead, dislocations interact with them through Orowan

bowing. The resulting strength increase is modeled as [36]

$$\tau_{\theta'} = \frac{2}{\lambda} \left(\frac{Gb}{4\pi\sqrt{1-\nu}} \right) \ln \left(\frac{1.225 t_r}{b} \right). \tag{5}$$

Using this approach, the tested microstructures can thus be given an estimated bulk strength of value $\tau_{\mathrm{CRSS}} = \tau_{\mathrm{CRSS,\,Al}} + \tau_{\mathrm{SS}} + \tau_{\mathrm{GP}} + \tau_{\theta''} + \tau_{\theta'}$, where pure Al, the dominant obstacle type, and the remaining solid-solution contribution are used. The values thereby obtained are included in Fig. 4(b) and show good agreement with the experimental data for all but the AlCuθ'/θ microstructure. We understand this discrepancy by the fact that the sampled volume is not sufficiently large to truly represent an average strengthening due to a θ'/θ precipitate structure. Now much of the deforming volume has a free surface instead of being confined by nonshearable obstacles.

With these bulk values at hand, it becomes evident that the characteristic length scales listed in Table II are sufficiently averaged in the case of the AlCuSS, the AlCuGP, and the AlCuθ'' microstructures as to be in a size-independent regime. In other words, the AlCu microcrystals tested here are small volumes whose flow response is representative of bulk plasticity. To test this idea further, we conducted a test series of 5 μm diameter crystals of each microstructure and the averaged data are also shown in Fig. 4(b). Only in the case of pure Al is a clear size-dependent reduction in the average flow shear stress observed, whereas the binary microstructures exhibit identical flow stresses for both sample dimensions, supporting the view that we probe a size-independent flow behavior.

We return our attention to the pronounced strain excursions seen in Fig. 4(a). These abrupt strain increments are, in addition to the finite size strengthening, the second size effect at this sample scale [52]. We now construct the size statistics of all extracted dislocation avalanches from each microstructure and all stresses. To this end, we rely on the stress-integrated complementary cumulative distribution function (CCDF), which is defined as $C(S) = P(S \geqslant S_{\mathrm{set}}) = D \int_s^\infty P(S) dS$, or in other words the probability of a recorded event size S of being larger or equal in magnitude to a given size S_{set}, with D being a normalization prefactor. The CCDF is preferred over the PDF because it is defined for every value and does not require any binning of discrete data that can have subtle but important effects on subsequently performed distribution fitting. The data collected here are known to follow a power law or truncated power law (TPL), $P(S) \propto S^{-\alpha} e^{-\delta S}$, where α is the scaling exponent of the power law and $e^{-\delta S}$ an exponential cutoff function described by the parameter δ. The corresponding CCDF mathematically follows the same trend, being $C(S) \propto S^{-\tau} e^{-\mu S}$, with $\tau = \alpha - 1$ and μ yet a different nonuniversal parameter that describes the cutoff. Figure 5 summarizes the CCDF of the experimental data.

A strong variation of event-size statistics can be seen, admitting a TPL distribution for the case of pure Al and an exponential distribution describes the data for the AlCuθ'/θ microstructure. Roughly, a gradual suppression of long-range correlated and scale-free-like dislocation activity is observed in order from pure Al, AlCuSS, AlCuGP, and AlCuθ'', to AlCuθ'/θ. While the scaling exponent $\tau \approx 0.5$ (or $\alpha \approx 1.5$) would be in agreement with mean-field depinning [53], we emphasize here that this must be more a coincidence than
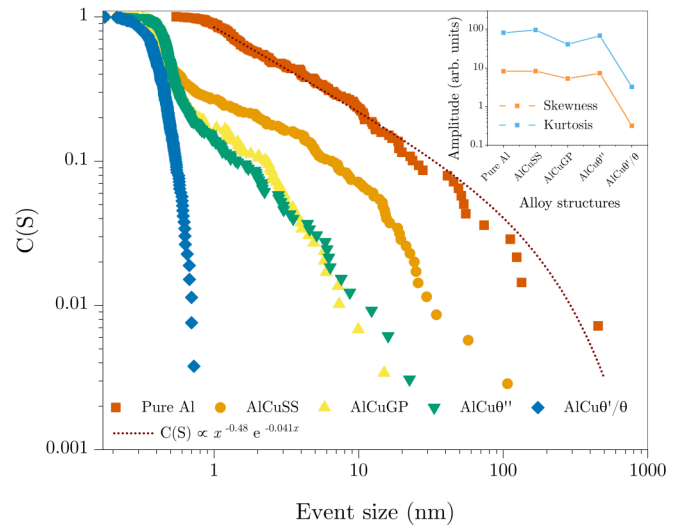

FIG. 5. CCDF of event sizes S for all considered structures. The evolution of event-size distribution is nontrivial and except for pure Al, they cannot be captured robustly with a given statistical function. Inset: Statistical moments (skewness, kurtosis) for all considered structures.

anything else, as both experiments [39] and modeling [54] have demonstrated the large variety of scaling exponents in the range of approximately $1 < \alpha < 2$. This range seems to be a result of a variety of boundary conditions, as well as the dynamical internal dislocation network evolution, and is more compatible with the jamming-unjamming framework [23]. Introducing a population of Cu atoms into the Al matrix clearly causes a significant drop of $C(S)$ for $S > 1$ nm. In other words, a substantial number of resolvable dislocation avalanches are now suppressed to the part of the distribution containing the smallest displacement magnitudes. Similarly, the largest events reduce their scale to ca. 100 nm, which is about an order of magnitude smaller than the truncation length scale for pure Al. This observation remains somewhat qualitative due to the inability of a meaningful fitting of the distribution. Attempts of fitting the overall data set for Al-CuSS with a weighted exponential and TPL distribution for the different size regimes did not yield robust results, which is due to the insufficient total range of S. This decrease of the truncation length scale is much less than reported for cluster formation in an Al 0.3 wt % Sc alloy with a majority of clusters in the size of 2–20 nm ($L_p \approx 20$), for which the event-size distribution truncates below 10 nm [24]. The contribution of the exponential shoulder at a low value of S increases for AlCuGP and AlCuθ'' but the fat-tail avalanche part at large S remains statistically indistinguishable for both cases. We note that the tail for these two microstructures approximates to a slope of unity that would be an exponent of 2 in the case of the PDF, which indeed is in good agreement with a prediction by Brown [55]. With the emergence of the θ'/θ precipitates, all correlated long-range interaction that would emerge via a strong PL or TPL contribution is lost, and avalanches now follow scale-dependent statistics best described by an exponential distribution. Essentially, the transition seen here in statistical behavior is much like a so-called mild-to-wild
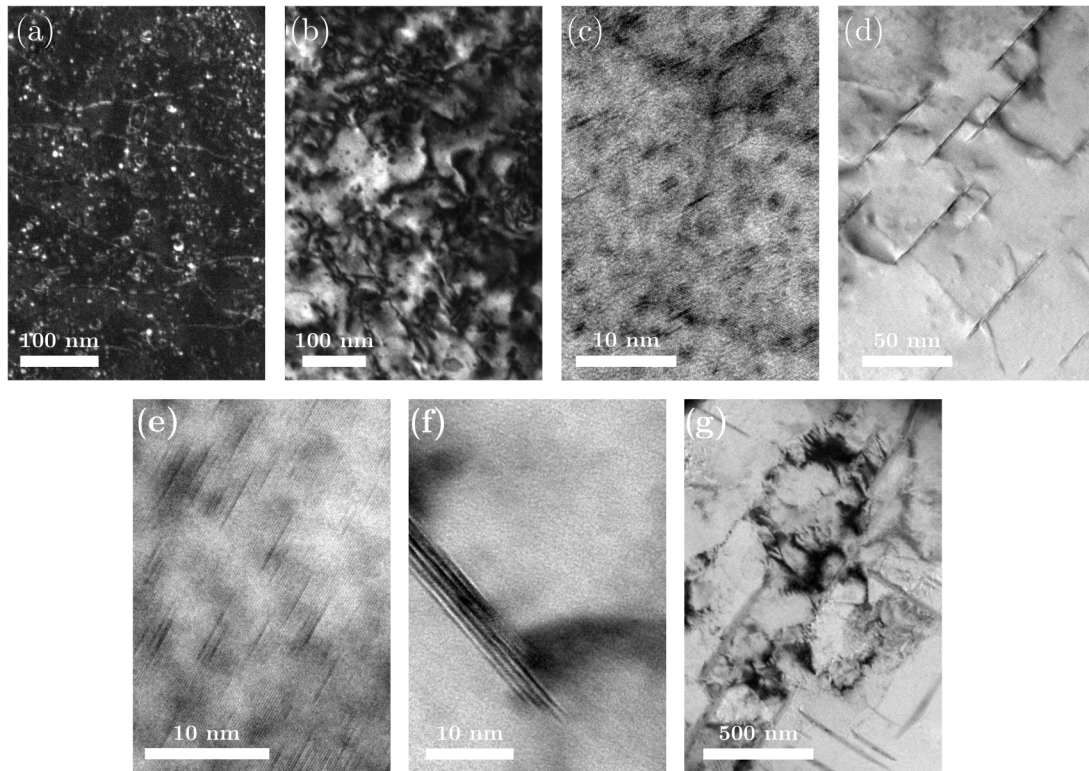
FIG. 6. TEM micrographs of dislocation behavior in each sample microstructure. (a) Dislocation density in pure Al after deformation (seen here in DF). (b) Dislocations in AlCuSS, where some amount of pinning is observed. (c) Dislocation lines being pinned at some GP zones. (d) Dislocations interacting with shearable θ'' precipitates in AlCuθ''. (e) Micrograph of AlCuGP structure showing the presence of GP zones throughout the entire sample. (f) Micrograph of AlCuθ'' featuring the edge of a precipitate but no GP zones are observed. (g) Dislocation-precipitate interaction in AlCuθ'/θ. Impenetrable precipitates cause pockets of high dislocation densities and pile up, suppressing correlated long-range interaction.

transition discussed earlier [56]. We note that the underlying dislocation activity for the θ'/θ microstructure still is weakly correlated, since the avalanche statistics does not transition to a pure Gaussian form [57,58]. A moment analysis for the different distributions captures this change from scale-free to scale-dependent statistics clearly via a marked change in both kurtosis (fourth normalized moment) and skewness (third normalized moment) once fully incoherent precipitates are present (inset in Fig. 5). This trend is qualitatively compatible with earlier work focusing on the finite sample size variation across an AlCuθ' microstructure with 2.5 wt % ($L_p \approx 1000$ nm) and 4.0 wt % Cu ($L_p \approx 700$ nm) and therefore significantly larger L_p values [25] that are approaching the sample dimension. In Ref. [25] the tail structure of the distributions was approximated with a PL, of which the scaling exponent increased strongly with decreasing L_p for this particular precipitate type.

How can this transition to a finite avalanche size scale be understood? Long-range correlated collective dislocation dynamics with scale-free avalanche statistics in pure metallic systems is now an established phenomenon in this type of microplasticity [3]. A specific microstructural length scale correlating with either the scaling exponent or the truncation length scale has so far not been identified for pure metallic systems that only contain an evolutionary dislocation network. This also agrees with work proposing a model that links the fraction of intermittently admitted strain to the scaling

exponent for a variety of AlSc and AlCu alloys [24,25]. Without the presence of quenched disorder (static pinning sites), it continues to remain unclear what property of the existing and evolving microstructure determines α or the truncation term μS. Indeed, TEM investigations yield a typical picture of a well-established dislocation network for the deformed microcrystals, as displayed in Fig. 6(a). Estimating the dislocation density for the undeformed and deformed Al yields ca. 5×10^{12} m^{-2} (equivalent to a mean spacing of 445 nm) and ca. 8×10^{13} m^{-2} (mean spacing of 110 nm), respectively.

The introduction of quenched disorder via the solution of Cu does alter this behavior, but clearly long-range coupling and avalanching over length scales orders of magnitude larger than the solute spacing still remains a strong part of the network evolution. Now TEM micrographs reveal the expected pinned dislocation lines in the deformed microcrystals [Fig. 6(b)]. Those events underlying the emerging shoulder at low S for AlCuSS are just above the resolution limit and admit slip equivalent to $0.4-0.8$ nm in net magnitude; a length scale that in fact is in good agreement with the average spacing of the introduced Cu solutes. Depleting the matrix of Cu and forming AlCuGP and AlCuθ'' introduces microstructural length scales of very different magnitude (Table II). Despite the order of magnitude larger precipitates and their distances, both microstructures exhibit the same avalanche-size distribution $C(S)$ in Fig. 5. Postmortem TEM micrographs [Figs. 6(c) and 6(d)] reveal dislocation lines crossing the GP and

precipitate structure and no particular change of $C(S)$ is observed. Both the size and the distances of the θ'' structure are at or beyond the truncation of the distribution. In both AlCuGP and AlCuθ'', however, the shoulder at low S remains, which is understandable as sufficient Cu remains dissolved in the matrix. Given this similar avalanche distribution, one may ask if the AlCuθ'' still contains a population of GP zones, which could be the dominant obstacle population controlling $C(S)$. To verify this, TEM micrographs from both initial microstructures are examined, paying attention to any possible signature of GP zones in the AlCuθ'' alloy. Figures. 6(e) and 6(f) demonstrate that the tested AlCuθ'' alloy was sufficiently aged as to dissolve all GP zones. This leads to the conclusion that $C(S)$ is experimentally indistinguishable for both microstructures due to the shearability of their precipitates. In view of the result by Sun and co-workers [24,25], where the fraction of plasticity due to intermittent events is linked to the ratio between the sample diameter and a length scale $l = Gb/\tau_{\text{pin}}$, with G being the shear modulus, b the Burgers vector, and τ_{pin} the effective pinning strength of the obstacles, $C(S)$ for AlCuGP and AlCuθ'' would be expected to differ due to different τ_{pin} (Table II lists both τ_{pin} and l for the here investigated alloys). This is not the case, which, however, may be drowned out in the large scatter of the data underlying the proposed model.

Once incoherent, the precipitates in AlCuθ'/θ can no longer be sheared anymore and significant pileup can be observed in the interprecipitate regions. This leads to confined regions of strong plastic activity, whereas other interprecipitate regions show no dislocation accumulation in postmortem TEM micrographs [Fig. 6(g)]. With the center-to-center distance still being smaller than the microcrystal diameter, selected sample subvolumes accommodate the far-field stress via intense dislocation activity without being able to develop sufficient collective behavior as to admit large instantaneous slip events. We note that the fraction of strain (or displacement) admitted by resolvable discrete plastic events is still between 10% and 20%, even though such discrete events have no scale-free-like statistics. As such, the gradual reduction in truncation length and the change for scale-free to scale-dependent avalanche statistics seen in Fig. 5 seems to be dictated by the nature of the microstructural obstacles (pinning strength, shearable vs not shearable), whereas their introduced length scale matters little.

IV. CONCLUSION

How microstructural length scales and specific obstacle types affect the correlated-collective dislocation motion that underlies intermittent plastic events in the form of dislocation avalanches continues to remain unclear. Here we observe a systematic transition from a correlated scale-free-like to a still correlated but scale-dependent statistical signature of intermittency when probing the microplastic response of Al and a variety of microstructures produced via controlled annealing of an Al 4.85 wt % Cu binary alloy. The simplest deviation from pure Al is the addition of Cu as a supersaturated solid solution, for which the avalanche distribution continues to have a strong power-law-like tail admitting avalanche sizes orders of magnitude beyond the character-

istic length scale of the solid solution. In coexistence with this continued long-range correlated-collective dislocation activity, a marked contribution of short-range interactions emerges in the size distribution. In this case, being an ideal model of a static pinning field, the strong signature of small avalanche sizes manifests itself at the same length scale as characteristic for the solid solution. For all other microstructures that contain different types of precipitates and characteristic length scales, such a correspondence cannot be observed. Instead, a continued suppression of the high-value tail (power-law signature) seems to be governed by the shearability of the microstructural obstacles rather than their related length scales or pinning strength. This is in qualitative agreement with dislocation dynamics simulations, in which only the introduction of a sufficiently high pinning strength eventually suppresses the critical (scale-free) dynamics [59]. While the present work cannot precisely account for the pinning strength distribution of the complex microstructures, in which a combination of a solid solution and a precipitate type always prevails, we conclude that scale-free dislocation avalanche dynamics in similar fcc systems with clear microstructural length scales occurs simultaneously with weakly correlated and scale-dependent non-Gaussian activity as long as penetrable interfaces (lattice coherency) exist. The same must apply to hexagonal closed packed polycrystalline metals containing a boundary network, for which signatures of intermittent avalanche activity still can be revealed [7,26]. These collected experimental observations add to reports demonstrating changes from scale-free to scale-dependent intermittency due to the stress state [12], as well as a temperature-dependent suppression of critical avalanche dynamics due to an increasing dominance of the lattice friction in bcc metals [60], all of which reinforce the notion of intricate nonuniversal and microstructural-specific avalanche dynamics. Overall, it becomes increasingly clear that Gaussian and non-Gaussian dislocation activities coexist, and that the latter includes the extreme dislocation events that may be rare but that can trigger significant local stress singularities. Even though dislocation self-organization and patterning can suppress the non-Gaussian correlated activity during deformation, it emerges again prior to failure, giving strong indications for its critical role in triggering failure [61,62]. These recent insights and the here observed statistical transition due to the microstructure in complex engineering alloys urge for continued fundamental efforts that take into account the coexistence of Gaussian and non-Gaussian defect behaviors such that metallurgical failure prediction eventually embraces both statistical components.

[1] E. Schmid and M. A. Valouch, Z. Phys. **75**, 531 (1932).

[2] O. Haase and E. Schmid, Z. Phys. **33**, 413 (1925).

[3] R. Maass and P. M. Derlet, Acta Mater. **143**, 338 (2018).

[4] E. Nadgornyi, Prog. Mater Sci. **31**, 1 (1988).

[5] D. M. Dimiduk, C. Woodward, R. Lesar, and M. D. Uchic, Science **312**, 1188 (2006).

[6] J. Weiss and J. R. Grasso, J. Phys. Chem. B **101**, 6113 (1997).

[7] K. Chatterjee, A. J. Beaudoin, D. C. Pagan, P. A. Shade, H. T. Philipp, M. W. Tate, S. M. Gruner, P. Kenesei, and J. S. Park, Struct. Dyn. **6**, 014501 (2019).

[8] A. A. Shibkov, M. F. Gasanov, M. A. Zheltov, A. E. Zolotov, and V. I. Ivolgin, Int. J. Plast. **86**, 37 (2016).

[9] C. C. Vu and J. Weiss, Phys. Rev. Lett. **125**, 105502 (2020).

[10] G. Sparks and R. Maass, Acta Mater. **152**, 86 (2018).

[11] Q. Rizzardi, G. Sparks, and R. Maass, JOM **70**, 1088 (2018).

[12] J. Shimanek, Q. Rizzardi, G. Sparks, P. M. Derlet, and R. Maass, J. Mater. Res. **35**, 196 (2020).

[13] M. Zaiser, J. Schwerdtfeger, A. S. Schneider, C. P. Frick, B. G. Clark, P. A. Gruber, and E. Arzt, Philos. Mag. **88**, 3861 (2008).

[14] A. I. Hegyi, P. D. Ispanovity, M. Knapek, D. Tuzes, K. Mathis, F. Chmelik, Z. Dankhazi, G. Varga, and I. Groma, Microsc. Microanal. **23**, 1076 (2017).

[15] J. Weiss and D. Marsan, Science **299**, 89 (2003).

[16] G. Sparks, P. S. Phani, U. Hangen, and R. Maass, Acta Mater. **122**, 109 (2017).

[17] M. C. Miguel, A. Vespignani, S. Zapperi, J. Weiss, and J. R. Grasso, Nature (London) **410**, 667 (2001).

[18] G. Sparks, Y. Cui, G. Po, Q. Rizzardi, J. Marian, and R. Maass, Phys. Rev. Materials **3**, 080601(R) (2019).

[19] G. Sparks and R. Maass, Phys. Rev. Materials **2**, 120601(R) (2018).

[20] M. Zaiser, Adv. Phys. **55**, 185 (2007).

[21] S. Zapperi and M. Zaiser, Mater Sci. Eng. **309**, 348 (2001).

[22] M. Ovaska, L. Laurson, and M. J. Alava, Sci. Rep. **5**, 10580 (2015).

[23] P. D. Ispanovity, L. Laurson, M. Zaiser, I. Groma, S. Zapperi, and M. J. Alava, Phys. Rev. Lett. **112**, 235501 (2014).

[24] P. Zhang, O. U. Salman, J.-Y. Zhang, G. Liu, J. Weiss, L. Truskinovsky, and J. Sun, Acta Mater. **128**, 351 (2017).

[25] P. Zhang, J. J. Bian, J. Y. Zhang, G. Liu, J. Weiss, and J. Sun, Mater. Des. **188**, 108444 (2020).

[26] T. Richeton, J. Weiss, and F. Louchet, Nat. Mater. **4**, 465 (2005).

[27] Q. Rizzardi, P. M. Derlet, and R. Maass, Phys. Rev. Materials **5**, 043604 (2021).

[28] M. Ovaska, T. Paananen, L. Laurson, and M. J. Alava, J. Stat. Mech.:Theory Exp. (2016) 043204.

[29] S. Papanikolaou, H. Song, and E. Van der Giessen, J. Mech. Phys. Solids **102**, 17 (2017).

[30] J. Alstott, E. Bullmore, and D. Plenz, PLoS One **9**, e85777 (2014).

[31] S. P. Ringer and K. Hono, Mater. Charact. **44**, 101 (2000).

[32] H. Sehitoglu, T. Foglesong, and H. J. Maier, Metall. Mater. Trans. A **36**, 749 (2005).

[33] J. G. Byrne, M. E. Fine, and A. Kelly, Philos. Mag. **6**, 1119 (1961).

[34] D. Vaughan and J. M. Silcock, Phys. Status Solidi **20**, 725 (1967).

[35] J. L. Murray, Int. Met. Rev. **30**, 211 (1985).

[36] J. F. Nie and B. C. Muddle, Acta Mater. **56**, 3490 (2008).

[37] J. F. Nie, B. C. Muddle, and I. J. Polmear, The effect of precipitate shape and orientation on dispersion strengthening in high strength aluminium alloys, *Aluminium Alloys - ICAA5*, Materials Science Forum, Vol. 217 (Trans Tech Publications, Lebanon, NH, 1996), pp. 1257–1262 .

[38] A. Rodríguez-Veiga, B. Bellón, I. Papadimitriou, G. Esteban-Manzanares, I. Sabirov, and J. Llorca, J. Alloys Compd. **757**, 504 (2018).

[39] J. da Costa Teixeira, D. G. Cram, L. Bourgeois, T. J. Bastow, A. J. Hill, and C. R. Hutchinson, Acta Mater. **56**, 6109 (2008).

[40] J. Zander and R. Sandstrom, Mater. Des. **29**, 1540 (2008).

[41] A. Biswas, D. J. Siegel, C. Wolverton, and D. N. Seidman, Acta Mater. **59**, 6187 (2011).

[42] R. Maass and M. D. Uchic, Acta Mater. **60**, 1027 (2012).

[43] S. I. Rao, D. M. Dimiduk, M. Tang, T. A. Parthasarathy, M. D. Uchic, and C. Woodward, Philos. Mag. **87**, 4777 (2007).

[44] M. D. Uchic, D. M. Dimiduk, J. N. Florando, and W. D. Nix, Science **305**, 986 (2004).

[45] H. Salmenjoki, A. Lehtinen, L. Laurson, and M. J. Alava, Phys. Rev. Materials **4**, 083602 (2020).

[46] T. A. Parthasarathy, S. I. Rao, D. M. Dimiduk, M. D. Uchic, and D. R. Trinkle, Scr. Mater. **56**, 313 (2007).

[47] J. R. Greer and J. T. M. De Hosson, Prog. Mater Sci. **56**, 654 (2011).

[48] A. J. Ardell, Metall. Trans. A **16**, 2131 (1985).

[49] A. Abel and R. K. Ham, Acta Metall. **14**, 1489 (1966).

[50] Z. Zhu and M. J. Starink, Mater. Sci. Eng.: A **489**, 138 (2008).

[51] J. F. Nie and B. C. Muddle, J. Phase Equilib. **19**, 543 (1998).

[52] P. M. Derlet and R. Maass, Philos. Mag. **95**, 1829 (2015).

[53] J. T. Uhl, S. Pathak, D. Schorlemmer, X. Liu, R. Swindeman, B. A. W. Brinkman, M. LeBlanc, G. Tsekenis, N. Friedman, R. Behringer *et al.*, Sci. Rep. **5**, 16493 (2015).

[54] T. Niiyama and T. Shimokawa, Phys. Rev. E **91**, 022401 (2015).

[55] L. M. Brown, Philos. Mag. **96**, 2696 (2016).

[56] J. Weiss, W. B. Rhouma, T. Richeton, S. Dechanel, F. Louchet, and L. Truskinovsky, Phys. Rev. Lett. **114**, 105504 (2015).

[57] P. Chaudhuri, L. Berthier, and W. Kob, Phys. Rev. Lett. **99**, 060604 (2007).

[58] X. Liang, J. Zhao, L. Dong, and K. Xu, Sci. Rep. **3**, 2983 (2013).

[59] H. Salmenjoki, L. Laurson, and M. J. Alava, Mater. Theory **4**, 5 (2020).

[60] Q. Rizzardi, C. McElfresh, G. Sparks, D. D. Stauffer, J. Marian, and R. Maass, Nat. Commun. **13**, 1010 (2022).

[61] J. Weiss, W. Ben Rhouma, S. Deschanel, and L. Truskinovsky, Phys. Rev. Materials **3**, 023603 (2019).

[62] I. V. Lomakin, T. Mäkinen, K. Widell, J. Savolainen, S. Coffeng, J. Koivisto, and M. J. Alava, Phys. Rev. Research **3**, L042029 (2021).